

Deciphering the structure and dynamics/kinetics in the performance enhancement of Lithium titanate in Li^+/Na^+ dual-cation electrolyte

Yue Chen ^{a, b, 1}, Shaohua Zhang ^{a, c, 1*}, Dongni Zhao ^d, Zhixian You ^{a, e}, Yubiao Niu ^f, Liqiang Zeng ^{a, e}, Nagarathinam Mangayarkarasi ^g, Oleg V. Kolosov ^g, Yongping Zheng ^{a, e}, Long Zhang ^{a, b, *}, and Zhigao Huang ^{a, b, e*}

^a College of Physics and Energy, Fujian Normal University, Fujian Provincial Key Laboratory of Quantum Manipulation and New Energy Materials, Fuzhou, 350117, China

^b Fujian Provincial Engineering Technical Research Centre of Solar-Energy Conversion and Stored Energy, Fuzhou, 350117, China

^c College of Physical Science and Technology, Xiamen University, Xiamen, 361000, China

^d Department of Chemistry, Energy Lancaster and Materials Science Institute, Lancaster, LA1 4YB, UK

^e Fujian Provincial Collaborative Innovation Centre for Advanced High-Field Superconducting Materials and Engineering, Fuzhou, 350117, China

^f We Are Nium Ltd. Research Complex at Harwell (RCaH), Rutherford Appleton Laboratory, Harwell, Didcot, OX11 0FA, UK

^g Physics Department, Lancaster University, Lancaster, LA1 4YB, UK

¹ Y. C. and S. Z. contribute equally. *Corresponding author: shzhang07@163.com; longzhang2023@163.com; zghuang@fjnu.edu.cn

Abstract

The widespread application of $\text{Li}_4\text{Ti}_5\text{O}_{12}$ (LTO) anode in lithium-ion batteries has been hindered by its relatively low energy density. Here, we investigate the capacity enhancement mechanism of LTO anode through the incorporation of Na^+ cations in the Li^+ -based electrolyte (dual-cation electrolyte). LTO thin film electrodes were prepared as conductive additive-free and binder-free model electrodes. Electrochemical performance assessments reveal that the dual-cation electrolyte boosts the reversible capacity of the LTO thin film electrode, attributable to the additional pseudo-capacitance and intercalation of Na^+ into the LTO lattice. *Operando* Raman spectroscopy validates the insertion of Li^+/Na^+ cations into the LTO thin film electrode, and the cation migration kinetics were confirmed by *ab initio* molecular dynamic (AIMD) simulation and electrochemical impedance spectroscopy (EIS), which reveals the incorporation of Na^+ reduces the activation energy of cation diffusion within the LTO lattice and improves the rate performance of LTO thin film electrodes in the dual-cation electrolyte. Furthermore, the interfacial charge transfer resistance in the dual-cation electrolyte, associated with ion de-solvation processes and traversal of the cations in the solid-electrolyte interphase (SEI) layer, are evaluated by distribution of relaxation time (DRT), Fourier transform infrared spectroscopy (FTIR) and X-ray photoelectron spectroscopy (XPS). Our approach of performance enhancement using dual-cation electrolytes can be extrapolated to other battery electrodes with sodium/lithium storage capabilities, presenting a novel avenue for the performance enhancement of lithium/sodium-ion batteries.

Keywords: Lithium titanate, Dual-cation electrolyte, *Operando* Raman, Distribution of relaxation time

1. Introduction

Lithium titanate ($\text{Li}_4\text{Ti}_5\text{O}_{12}$ or LTO) serves as a prevalent anode material in lithium-ion batteries[1], with charge primarily stored within LTO through the $\text{Li}_4\text{Ti}_5\text{O}_{12}$ (Li_4) \rightleftharpoons $\text{Li}_7\text{Ti}_5\text{O}_{12}$ (Li_7) phase transition. This phase transition, from Li_4 to Li_7 , demonstrates minimal volume expansion (<0.2%) during lithium insertion/extraction, earning LTO the nickname/title “zero-strain anode material”. Additionally, during lithiation and de-lithiation of LTO within the voltage range of 3.0-1.1 V vs Li^+/Li , the surface of the LTO electrode remains stable against the reductive decomposition of the electrolyte, resulting in the minimal formation of a solid-electrolyte interphase (SEI) film. The zero-strain attribute, coupled with the limited SEI formation, contributes to the long-term stability of LTO as a battery material. However, LTO exhibits a theoretical capacity of merely 175 mAh g^{-1} within the voltage range of 3.0-1.1 V versus Li^+/Li , which stands as a primary drawback compared to the commonly employed commercial graphite anode electrodes, limiting its broader application.

Numerous researchers have devised optimization strategies to enhance the specific capacity of LTO. These include widening the voltage range for charge/discharge to 3.0-0.1 V[2], a modification that elevates the theoretical specific capacity of lithium titanate to more than 200 mAh g^{-1} . Alternatively, the extra lithium storage capability has been tapped via strategies that include nanostructure and crystalline phase regulation[3], elemental doping[4-7], induction pseudocapacitive effect[8] and oxygen vacancies[9], and optimizing the crystal orientation[10]. Nevertheless, electrolyte engineering is assumed to be more effective than electrode modification in terms of cost, manufacturing, and scalability. However, there exists a notable gap in the literature regarding this strategy[11, 12]. Currently, electrolyte engineering in LTO material is primarily focused on optimizing anions and solvents, additives to alter solvation structures, reducing de-solvation energy, inhibiting gas production and facilitating the formation of SEI films at low potential regions to enhance rate performance[13]. Interestingly, multi-cation lithium-ion battery electrolytes, in which the electrolyte solution contains more than one type of cation in addition to Li^+ [14], have been reported to enhance the performance and safety characteristics of lithium-ion batteries by leveraging the unique properties of different cations[15]. The inclusion of additional cations, such as sodium ions (Na^+), potassium ions (K^+), or magnesium ions (Mg^{2+}), can improve the conductivity, stability, and cyclability of the electrolyte, resulting in a higher battery performance. While lithium and sodium ions share similar physical and chemical properties, their different ion sizes and electronegativities may lead to distinct electrochemical reactivity and ionic migration kinetics in the LTO lattice. The lack of research on the optimization of cations in electrolyte and the knowledge gained from the literature that the synergistic effect of dual ions in improving the migration kinetics motivated our exploration of the Li^+/Na^+ dual-

cationic electrolyte[16] which is designed to unleash the additional capacity of the LTO electrode.

LTO has been demonstrated to have a decent Na⁺ storage capacity, promising it as a sodium-ion battery material[17-20]. Yu et al performed the charge storage analysis of Na⁺ in an LTO anode, suggesting that Na⁺ can be stored at defects on the LTO nanocrystalline surface through pseudocapacitive charge storage, offering a promising solution for high-capacity and high-rate insertion sodium ion battery and without compromising structural integrity[8]. However, Sun and Kitta et al used in-situ XRD to study the phase composition changes during the sodiation and de-sodiation of LTO, manifesting a three-phase separation mechanism induced by Na⁺ intercalation into LTO lattice[18] [21]. Moreover, it has been pointed out that the storage of Na⁺ in LTO is a solid-solution phase transition mechanism at low charge/discharge rates and a two-phase transition mechanism at high rates[22]. Overall, the mechanism of Na⁺ embedding and surface pseudo-capacitance (intrinsic or non-intrinsic pseudo-capacitance) are still under debate[8, 23] due to the absence of effective lattice-scale operando characterization techniques for the determination of the Na⁺ occupancy sites and embedding mechanism[21, 24]. Since Na⁺ has a relatively larger ion size compared with Li⁺, it has been reported that Na⁺ embedded in the LTO lattice was monitored by XRD[22, 25] and confirmed that part of the capacity is contributed by the sodium intercalations. In addition, Wei et al identified the non-intrinsic pseudocapacitive effect of Na⁺ adsorption on the LTO surface as a major capacity contributor for sodium storage[23]. Unfortunately, in the absence of co-confirmation of other high-resolution techniques[26], it is difficult to determine the specific sodium intercalation or adsorption sites.

Hence, in this study, a binder-free LTO thin film electrode was prepared to study the charge storage mechanism and lattice structure evolution of LTO in Li⁺/Na⁺ dual-cation electrolyte in detail using *operando* Raman spectroscopy. The results showed that sodium ions initially occupied 8a sites and finally moved to the 16c sites. Electrochemical performance testing revealing that it is the sodium pseudocapacitive intercalation and adsorption proved the additional capacity for LTO. Additionally, the ion migration in LTO lattice bulk and interface are studied in detail to reveal the novel electrochemical behaviour of LTO in dual-cation electrolytes, offering new insights for improving battery capacity using dual-cation electrolytes.

2. Experimental section

2.1 Preparation of lithium titanate thin films

The LTO thin film model samples were prepared by magnetron sputtering using polished stainless-steel sheets as substrates. The LTO target was sputtered in an atmosphere of 0.5 Pa argon-oxygen mixture (Ar₂: O₂ = 4:1) for 4 hours to obtain an amorphous LTO film, and then the model electrode

1 was annealed at 700°C in a 0.5 Pa argon environment for 4 hours to form a crystalline LTO thin film
2 electrode. The electrochemical performance of LTO film electrodes was tested by assembling CR 2025
3 coin-cell batteries with LTO thin film electrodes as working electrodes and lithium foil/sodium foil as
4 reference and counter electrodes. The electrolytes were prepared by mixing different ratios of 1 M
5 LiPF₆ in Ethylene carbonate (EC): diethyl carbonate (DEC) = 1:1 and 1 M NaPF₆ in EC: DEC = 1:1
6 electrolyte.
7
8
9

10 **2.2 Structural characterization and electrochemical testing**

11 Cyclic voltammetry (CV) and electrochemical impedance spectroscopy (EIS) were tested by a
12 CHI660c potentiostat (CHI, USA) with a test window of open circuit potential (OCP)-0.35 V vs Li⁺/Li.
13 The LabRAM HR Evolution (*Operando* Raman spectrometer) is used to study the occupied state of
14 lithium/sodium ions. *Operando* Raman spectra during ion intercalation were measured using an EL-
15 CELL (German ec-opto-std) by a 532 nm green laser. *In-situ* measurements were performed in a glove
16 box (MBraun, Germany) with oxygen and moisture content < 0.5 ppm. Electron microscope images
17 were carried out by scanning electron microscope (SEM) SU8010 (Hitachi, Japan) and transmission
18 electron microscope (TEM) TALOS F200X (Thermo Fisher Scientific, USA). The X-ray
19 photoelectron spectroscopy (XPS) uses a Kratos Analytical AXIS Supra spectrometer, a
20 monochromatic Al K α 1486.7 eV X-ray source, operating at 15 kV, 15 mA, and an electron gun for
21 charge neutralization. The cell disassembly, transfer and XPS testing processes were conducted in an
22 Argon-protective environment. All spectra were analysed using CASAXPS (Casa Software Ltd, UK).
23 The infrared spectra of different proportions of electrolytes were measured by Nicolet IS50 (Thermo
24 Fisher, USA). The surface topography and roughness of the as-deposited LTO thin film were
25 determined by Bruker dimension Icon (Bruker, USA) atomic force microscopy (AFM). Distribution
26 of relaxation time (DRT) analysis was used to deconvolute the specific electrochemical processes,
27 including the lithium-ion migration in LTO lattice bulk, shuttling through the electrode-electrolyte
28 interface, as well as de-solvation processes before entering the SEI layer. DRT use the transformation
29 equation: $Z(\omega) = R_{\infty} + \int_0^{\infty} \frac{\gamma(\tau)}{1+j\omega\tau} d\tau$, to display the frequency domain-based Nyquist plots into time
30 domain-based DRT spectra[27]. The full-range electrochemical impedance spectra will be converted
31 as a relaxation-based function $\gamma(\tau)$ [28, 29]. Peaks occurring at specific relaxation times denote the
32 corresponding specialized electrochemical processes, with peak areas reflecting impedance values.
33
34
35
36
37
38
39
40
41
42
43
44
45
46
47
48
49
50
51
52
53
54

55 **2.2 *ab initio* molecular dynamic (AIMD)**

56 Li₄Ti₅O₁₂ crystallizes in the cubic $Fd\bar{3}m$ space group (no. 227) with a spinel structure were used for
57 the AIMD simulations. We first relaxed the Li₄Ti₅O₁₂ lattice with and without Na⁺ dopants using
58
59
60
61
62
63
64
65

density functional theory (DFT) simulations with the Vienna *ab initio* Simulation Package (VASP). The simulations employed the generalized gradient approximation (GGA) and a cutoff energy of 520 eV with a PAW–PBE basis set. The optimized lattice parameters were found to be $a = b = c = 8.4 \text{ \AA}$. In these structures, Li^+ ions at 8a sites are bonded to four equivalent O^{2-} atoms, forming LiO_4 tetrahedra that share corners with twelve equivalent TiO_6 octahedra. The atomic-scale dynamics of $\text{Li}_4\text{Ti}_5\text{O}_{12}$ were performed by AIMD simulations using the Chgnet code[30] in a $1 \times 3 \times 1$ supercell of $\text{Li}_4\text{Ti}_5\text{O}_{12}$ consisting of 168 atoms. In the doped LTO lattice, 1/6 of the Li^+ at 8a sites are randomly substituted by Na^+ . The cation migration simulations were performed in the NVT ensemble, with temperatures ranging from 800 to 1400 K, using a Nose-Hoover thermostat to control the temperature. The time step was set to 2 fs, and the total simulation time was 100 ps. By analysing the trajectories generated from the AIMD simulations, we were able to elucidate the dynamic behaviour of lithium/sodium ions, titanium ions, and oxygen atoms in the LTO lattice. The simulations provided valuable insights into the material's electrochemical properties, including the diffusion mechanisms of cations and the structural changes induced by Na^+ substitutions.

3. Results and Discussion

3.1 Crystal and microstructure of LTO thin film model electrode

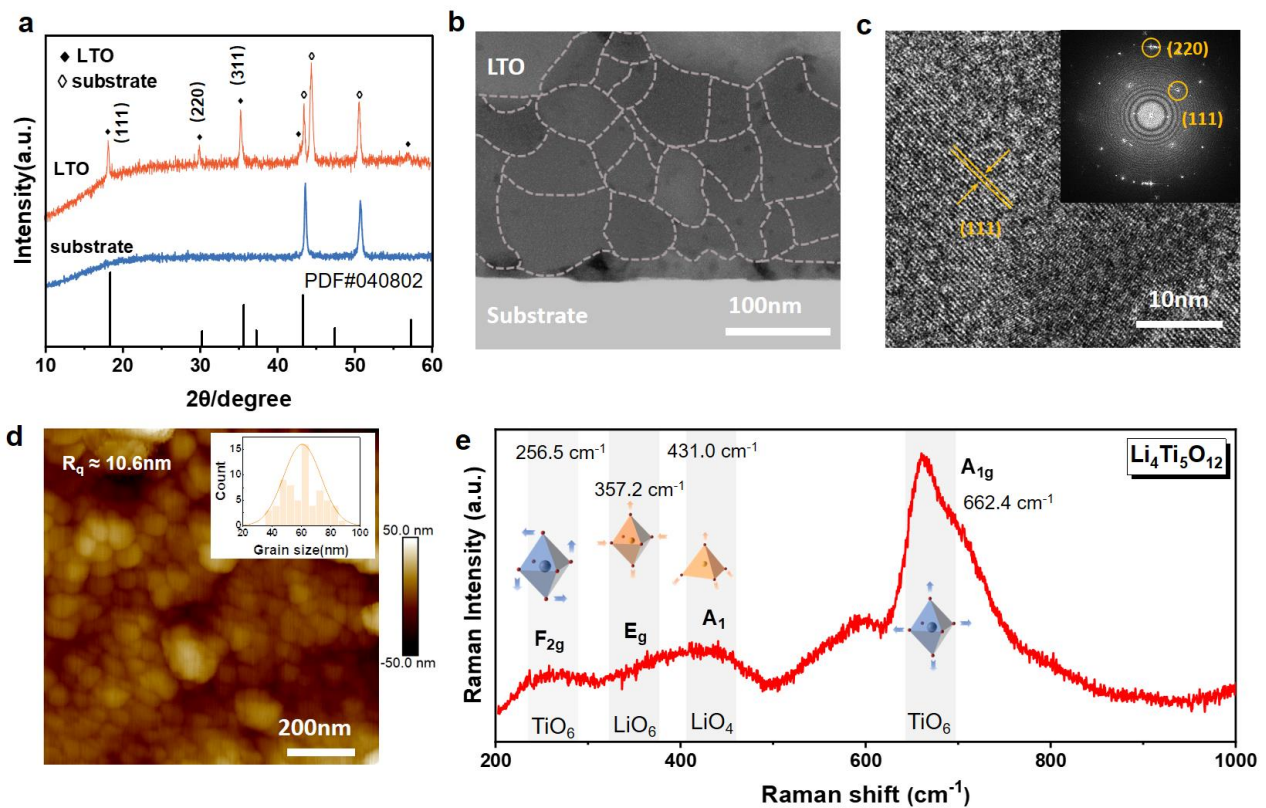


Figure 1 (a) XRD patterns and (b) cross-sectional SEM image of the as-deposited LTO thin film on the polished stainless-steel substrate. (c) High-resolution TEM image with fast Fourier transform pattern captured at the as-

deposited LTO layer. (d) AFM surface topography image of the as-deposited LTO thin film. (e) Raman spectra of the as-deposited LTO thin film electrode with the vibration schematic diagram of each labelled peak.

Figure 1a shows the XRD patterns of the as-deposited LTO thin film electrode and bare stainless-steel substrate. The XRD spectrum of the LTO thin film electrode contains the diffraction peaks at $2\theta = 18.3^\circ$, 30.6° and 42.9° , corresponding to the (111), (220) and (311) crystal planes of spinel LTO according to the PDF#-040802 standard card. This confirms that the as-prepared LTO films have good crystallinity with the $Fd\bar{3}m$ space group. Figure 1b is the cross-sectional SEM image of the as-deposited LTO film on the substrate. From the figure, it can be seen that the LTO film has a polycrystalline characteristic with many grain boundaries. High-resolution transmission electron microscopy (HRTEM) image shows clear lattice fringes with an interlayer spacing of about ~ 0.48 nm (Figure 1c), corresponding to the (111) crystal plane of spinel LTO. Figure 1d is the surface topography image measured by AFM, in which a flat electrode surface and well-crystallized grains can be observed. The surface roughness (R_q) and grain size obtained by statistical analysis are about 10.6 nm and 58.5 nm, respectively. In addition, the Raman spectra of the as-prepared LTO films are shown in Figure 1e. The peak at the wave number near 233cm^{-1} is the F_{2g} vibration mode[21], corresponding to the bending vibration of TiO_6 octahedrons. The peak at the wavenumber of about 335 cm^{-1} and 432 cm^{-1} can be attributed to the E_g mode vibrations derived from the bending vibrations of LiO_6 octahedrons and LiO_4 tetrahedrons, respectively[31, 32]. The peak at a high wavenumber area ($\sim 672\text{ cm}^{-1}$) corresponds to the symmetrical tensile vibration of the TiO_6 octahedron in the LTO crystal structure[21]. The characterization of these Raman peaks and the crystalline/nanostructure described above unambiguously supported that the as-prepared binder-free LTO thin film electrode has good crystallinity with $Fd\bar{3}m$ structure, and can be used as the ideal mode for the study of cation insertions.

3.2 Enhanced capacity of LTO anode and the charge storage mechanism

The galvanostatic cycle stability and rate performance of LTO thin film electrode in single-cation electrolyte (1 M LiPF_6 in EC: DEC = 1:1 v%) and dual-cation electrolyte (1 M LiPF_6 : NaPF_6 =1:1 in total in EC: DEC = 1:1 v%) were evaluated as shown in Figures 2a and 2b. One can observe in Figure 2a that, under 1 C charge/discharge rate, LTO in dual-cation can deliver a reversible capacity of about 190 mAh/g after 260 cycles, which is about 15% higher than the capacity cycled in the single Li^+ cation electrolyte. This confirms the enhanced cycle stability of the LTO thin film electrode when switching the electrolyte from a single-cation to a dual-cation electrolyte. Moreover, one can observe in Figure 2b that, the rate performance of LTO thin film electrodes cycling in dual-cation electrolytes is also higher than that of single-cation electrolytes. These electrochemical performance measurements unambiguously support that the dual-cation electrolyte improves the cycle stability and rate

performance of the LTO thin film anode compared with the conventional single-cation electrolyte.

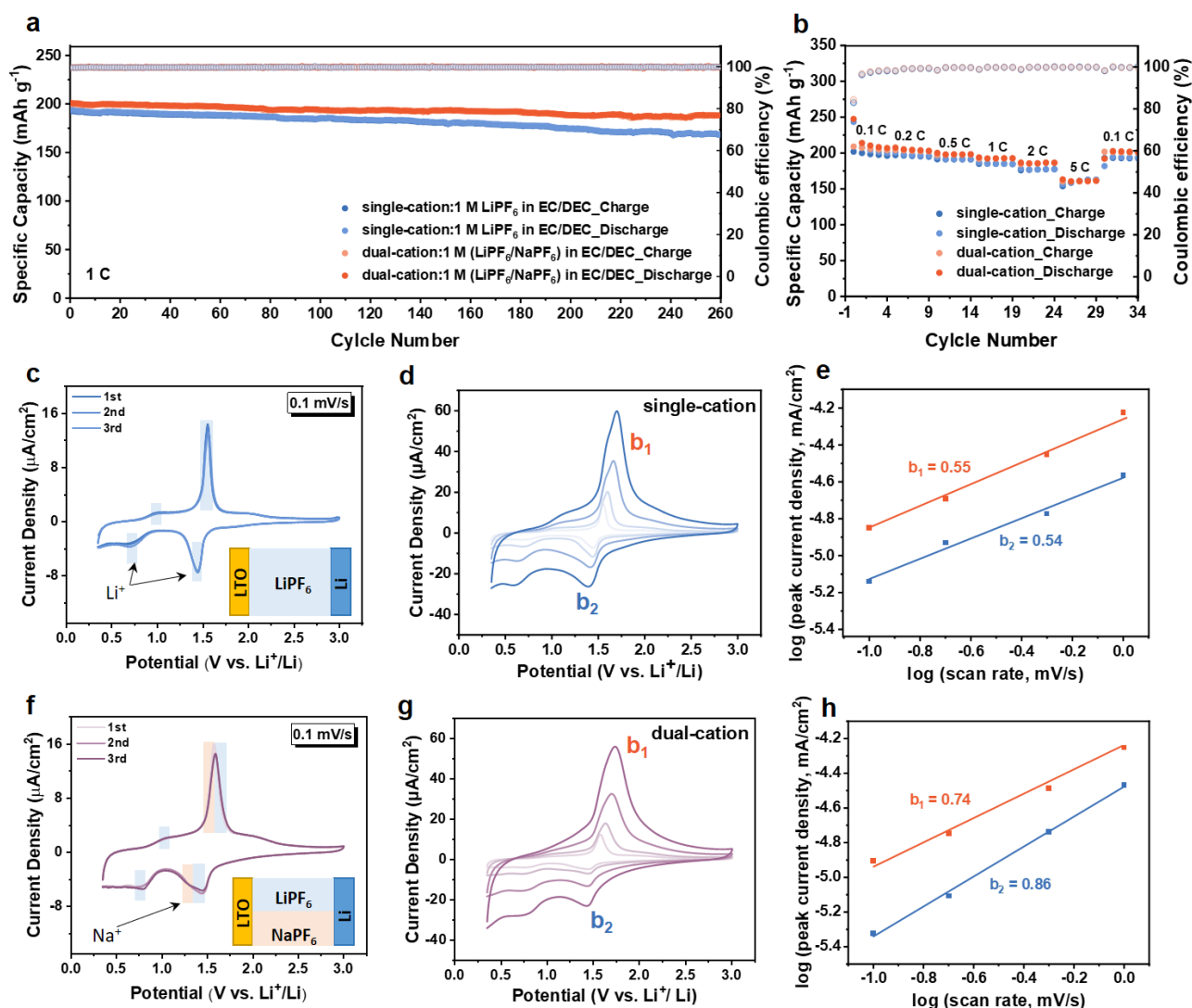
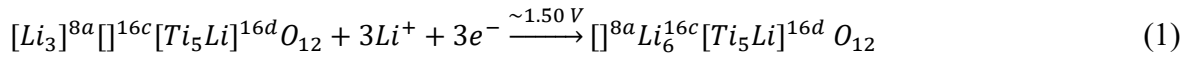


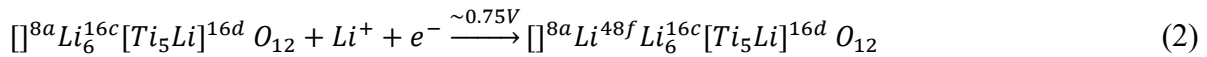
Figure 2 (a) Long-term cycle performance and (b) rate performance of LTO thin film electrode in single-cation electrolyte (1 M LiPF₆ in EC: DEC = 1:1) and dual-cation electrolyte (1 M LiPF₆: NaPF₆=1:1 in EC: DEC = 1:1). CV cycle curves of LTO in (c) single-cation electrolyte system and (f) dual-cation electrolyte system at slow sweep rate (0.1 mV s⁻¹). Variable-speed CV test of LTO in (e) single-cation electrolyte system and (g) dual-cation electrolyte system (sweep speed at 0.1 mV s⁻¹, 0.2 mV s⁻¹, 0.5 mV s⁻¹ and 1 mV s⁻¹). (g and h) The linear fits of the b-values of the two redox peaks (b₁, b₂) in (Figures 2c, and 2d), respectively.

Attempts have been made to differentiate the charge storage mechanisms in single and dual cation electrolyte systems by assigning the redox peaks of the CV performed at a slow scan rate for the binder-free LTO thin film electrodes. To reveal the underlying electrochemical reactions, we performed the CV tests with a slow scan rate for the binder-free LTO thin film electrodes, aiming at analysing the charge storage mechanisms in each system by the assignment of CV redox peaks. For the Li⁺ intercalation into LTO in the single-cation electrolyte, a reductive peak at ~1.50 V can be observed as

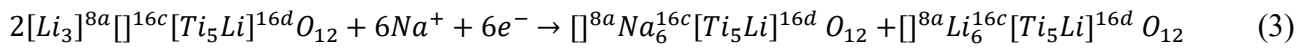
shown in Figure 2c. This can be attributed to the insertion of lithium ions into the 16c sites, followed by the lithium ions that originally stayed at 8a sites migrating to 16c sites due to the coulombic repulsive force. These Li⁺ insertions and migrations can be expressed as Eq. (1):



Upon further scanning down the electrode potential to around 0.75 V, the intercalated lithium ions may occupy other interstitial sites, such as empty 48f sites[33], providing additional capacity. This process also generates a pair of redox peaks at 0.75 V (reduction) and 0.92 V (oxidation) as shown in Figure 2c, whose ion migration and charge transfer processes can be expressed as:



The CV curves of the LTO thin film anode in the dual-cation electrolyte are shown in Figure 2f. Comparing Figures 2c and 2f, it can be seen that the addition of sodium ions results in an emerging new peak on the low-voltage side of the initial reductive peak (~1.50 V), as well as a widening of the corresponding oxidation peak. These new peaks can be attributed to the intercalation of sodium ions[34]:



To further differentiate the types of Faradaic contribution by Li⁺/Na⁺ cations, insertion or adsorption (i.e., pseudocapacitive effect)[35, 36], the CV tests at various scanning speeds of 0.1-2 mV s⁻¹ are conducted. The results are shown in Figures 2d and 2g. In the figures, by measuring the peak current (*i*) at various CV scanning speeds (*v*), the battery-type behaviour and pseudocapacitive-type behaviour can be distinguished. The measured peak current follows the relationship with the scanning speed[37]:

$$i(V) = av^b \quad (4)$$

where the peak current *i* is a function of the electrode potential *V*, which follows the power-law relation with the scan rate *v*. The *b*-value of 0.5 refers to an ideal semi-infinite diffusion process, and *b* = 1 indicates a surface-controlled or capacitor-like kinetics. Equation (5) can be obtained by taking log on both sides of the Equation (4),

$$\log i(V) = b \log v + \log a \quad (5)$$

where the value of *b* can be obtained by measuring the slope of the *log(i)* vs *log(v)* plots. Figures 2e and 2h are the result of the *b* value calculated by the peak current in CV curves. The *b* value for the LTO cycled in single-cation electrolyte is 0.5~0.6, indicating that the charge storage of Li⁺ in single-cation electrolyte mainly comes from the intercalation reactions. For the dual-cation battery system,

the b values corresponding to the two sets of redox peaks are higher than that of the pure lithium intercalation processes, especially the b_2 peak that has a value of about 0.86, indicating that there are additional surface-controlled capacitive contributions in the dual-cation electrolyte system. In other words, apart from the Na^+ intercalations, the dual-cation electrolyte brings an additional pseudocapacitive effect to the LTO thin film electrode, boosting the reversible capacity and high-rate performance.

3.3 Revealing the Li^+ and Na^+ crystal occupation states and migration kinetics

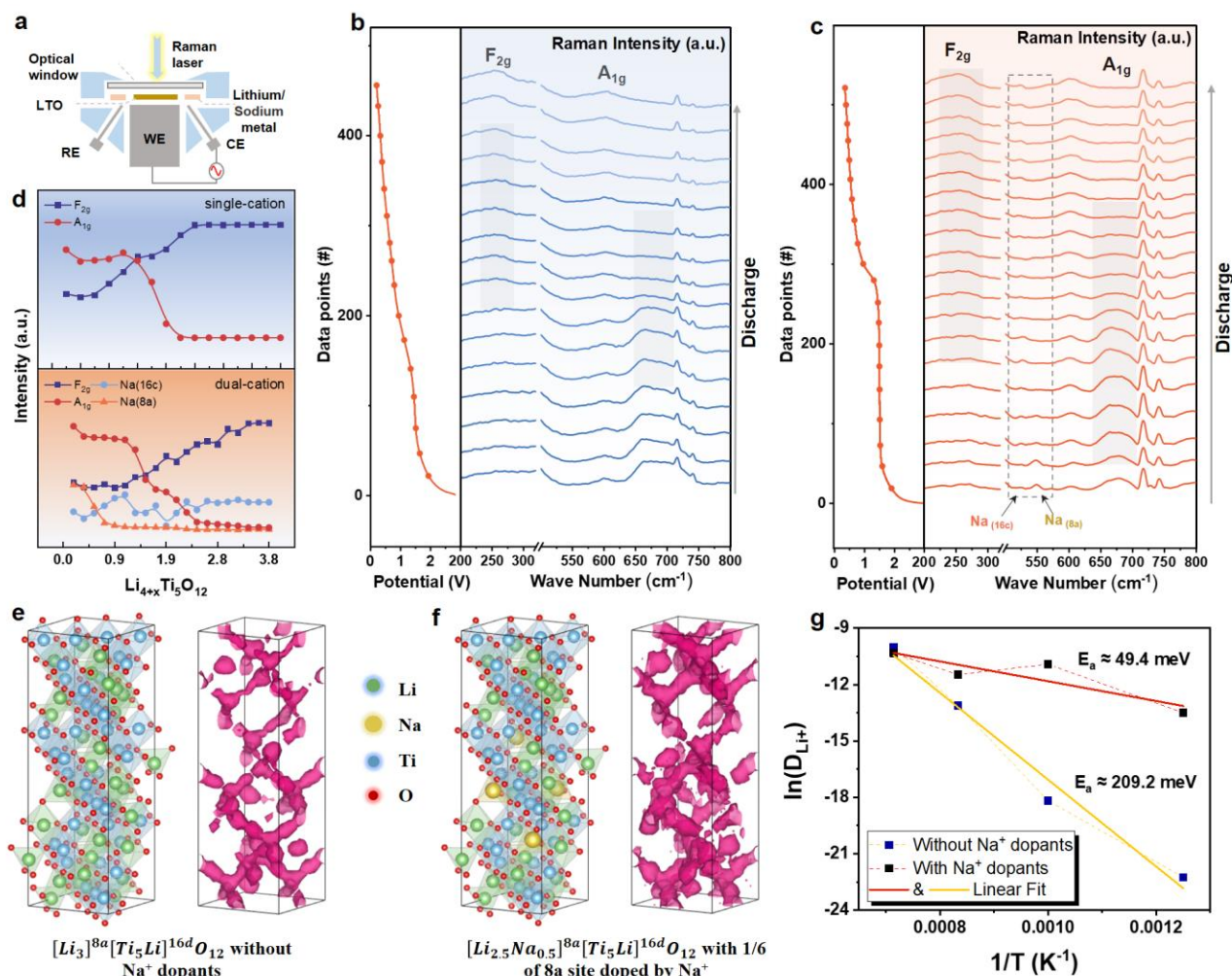


Figure 3 (a) Schematic diagram of the *operando* Raman test cell. *Operando* Raman spectra of LTO discharging in (b) a single cation (1 M LiPF_6 in EC: DEC = 1:1) and (c) a dual-cation (1 M LiPF_6 : NaPF_6 = 1:1 in EC: DEC = 1:1 electrolyte) electrolyte system. (d) The summarized characteristic Raman peak intensity evolutions are from Figures 3b and 3c. The atomic-scale crystal structures for AIMD simulations and the obtained ion migration channels for modelling the LTO electrode cycled in (e) single-cation and (f) dual-cation electrolyte. In the simulation model for LTO lattice cycled in dual-cation electrolyte, 1/6 of the Li^+ at initial 8a sites are substituted by Na^+ . (g) The calculated activation energies for cation migration within LTO lattice with and without Na^+ dopants.

1 To further study the ion intercalation within LTO thin film electrodes in the two types of electrolytes,
 2 *operando* electrochemical Raman spectra were measured using the electrochemical cell as shown in
 3 Figure 3a. The working electrode is LTO thin film electrodes, the counter and reference electrodes are
 4 lithium metals, and the electrolytes used in Figures 3b and 3c are the single-cation electrolyte and dual-
 5 cation electrolyte, respectively. The peak intensity evolution of the characteristic Raman band in
 6 Figures 3b and 3c are summarized in Figure 3d. As shown in the Raman spectra in Figure 3b and the
 7 summarized results in Figure 3d, upon the lithium-ion intercalation, the torsional vibration (F_{2g} peak
 8 at $\sim 243\text{ cm}^{-1}$) of the TiO_6 octahedron was enhanced, while the symmetrical tensile vibration (A_{1g} peak
 9 at $\sim 674\text{ cm}^{-1}$) of the TiO_6 octahedron[21] was suppressed. Although, with dual-cation electrolyte also
 10 had an increase of F_{2g} peak intensity and a decrease of A_{1g} peak intensity similar to the single-cation
 11 electrolyte, two new peaks at about 451 cm^{-1} and 500 cm^{-1} are observed (Figures 3c and 3d). The new
 12 peak at 500 cm^{-1} in dual-cation electrolyte appears at the beginning of the discharge but disappears
 13 quickly, which might correspond to the transient occupancy of Na^+ at the 8a sites, while the peak at
 14 low wavenumber may be attributed to the embedded Na^+ which eventually occupies the 16c sites,
 15 forming a phase with the structure of $[\text{Li}_{6-x}\text{Na}_x]^{16c}[\text{LiTi}_5]^{16d}\text{O}_{12}$ phase^[18]. Considering that at the
 16 end of discharge, lithium and sodium ions both occupy the 16c sites, and the total available 16c sites
 17 in the LTO anode are the same in the two electrolyte systems, we, therefore, believe the extra capacity
 18 in dual-cation electrolytes should either come from Na^+ intercalation at the interstitial sites or the
 19 adsorption at the defect sites.
 20
 21
 22
 23
 24
 25
 26
 27
 28
 29
 30
 31
 32
 33
 34

35 Raman spectra revealed that Na^+ ions initially intercalate and occupy the 8a sites, which could act as
 36 dopants that affect the Li^+ migration inside the LTO lattice. The lithium-ion migration kinetics within
 37 the LTO lattice with and without these initial Na^+ dopants were further evaluated using *ab initio*
 38 molecular dynamic (AIMD) simulations. Figures 3e and 3f show the crystal structures and simulated
 39 ion migration channels of LTO with and without Na^+ dopants at the 8a sites. In the initial LTO lattice
 40 without Na^+ dopants, the LTO has a structure of three $[\text{Li}_3]^{8a}[\text{Ti}_5\text{Li}]^{16d}\text{O}_{12}$ unit cells, in which
 41 the 1/6 of the Ti^{3+} at 16d sites in the octahedral TiO_6 (blue colour) are replaced by Li^+ , forming the
 42 LiO_6 octahedrons (green colour). While in the LTO lattice with Na^+ dopants, the Li^+ at the 8a site are
 43 further replaced by Na^+ , forming $[\text{Li}_{2.5}\text{Na}_{0.5}]^{8a}[\text{Ti}_5\text{Li}]^{16d}\text{O}_{12}$ structure with NaO_4 tetrahedrons
 44 (gold colour). Within these two crystal lattices, the *ab initio* molecular dynamic simulation was
 45 performed to visualize the cation migration channels and kinetics as shown in Figures 3e and 3f. The
 46 shapes of the corresponding ion migration channels in the LTO with and without Na^+ dopants are
 47 similar, both showing a 3D matrix connecting the tetrahedral and octahedral vacancy sites. However,
 48 the migration possibility of cations, which is proportional to the volumetric density of migration
 49
 50
 51
 52
 53
 54
 55
 56
 57
 58
 59
 60
 61
 62
 63
 64
 65

channels, in the $[Li_{2.5}Na_{0.5}]^{8a}[\]^{16c}[Ti_5Li]^{16d}O_{12}$ is higher than that in $[Li_3]^{8a}[\]^{16c}[Ti_5Li]^{16d}O_{12}$, indicating an activation effect of Na^+ dopants on the cation migrations within the LTO lattice. This may be attributed to the lower coulombic repulsive force between Na^+ and other cations. The calculated activation energies (Figure 3g) of cation migrations inside the LTO lattice with and without Na^+ dopants are about 49.4 meV and 209.2 meV, respectively. This increased cation migration capability, attributed to the Na^+ dopants, could be the key factor behind the enhanced rate performance of LTO in the dual-cation electrolyte.

3.4 Lithium transportation kinetics in LTO half-cell using single/dual-cation electrolytes

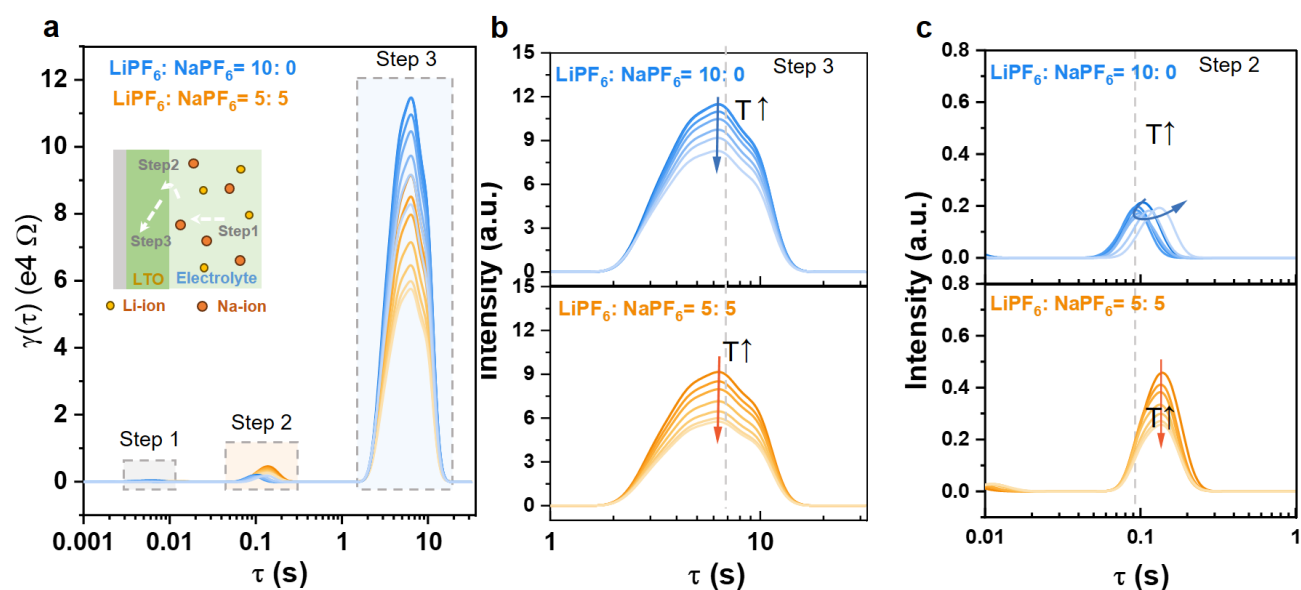


Figure 4 (a) Temperature-dependent DRT full spectra at 30°C, 35°C, 40°C, 45°C, 50°C, 55°C and 60°C (from dark to light traces) of LTO thin film anode in single-cation (blue) and dual-cation electrolyte (orange). The inset shows the schematic diagram of the three steps of lithium-ion migrations from the electrolyte to the LTO lattice. Zoom-in DRT spectra of LTO cell in single-cation and dual-cation electrolyte at the time constant region of (b) Step 3 and (c) Step 2.

To further understand the Li^+ transportation kinetics at the half-cell scale in single-cation and dual-cation electrolyte systems, various kinetic processes with specific relaxation features were identified and studied in timescales using the distribution of relaxation time (DRT) spectroscopy. Within LTO thin film half-cells, the transport of lithium ions unfolds in a series of three distinct steps as they travel from the electrolyte to the LTO lattice (see the inset in Figure 4a). The initial step (Step 1) entails the diffusion of lithium ions and lithium solvation complexes within the electrolyte bulk, facilitating their movement and subsequent adsorption onto the surface of the LTO electrode. After that, in the second step (Step 2), lithium ions undergo a de-solvation process wherein they shed solvent molecules and traverse the interface between the electrode and electrolyte. The last step (Step 3) involves the diffusion

1 of lithium ions within the intricate lattice structure of LTO. Temperature-dependent impedance
2 spectroscopy tests were conducted on the LTO half-cells with single-cation and dual-cation electrolytes
3 at temperatures of 30°C, 35°C, 40°C, 45°C, 50°C, 55°C, and 60°C. The obtained Nyquist plot was
4 converted to the DRT spectra as shown in Figure 4a. Three distinct DRT peaks are observed in both
5 cells. The first peak at the relaxation time of approximately 10^{-2} seconds corresponds to the ion
6 migration process in the electrolyte. The second peak, with a relaxation time of about 10^{-1} seconds, is
7 associated with an interfacial process involving solvent molecule de-solvation and traversal of the SEI
8 layer. The last peak, with a relaxation time of around 10 seconds, corresponds to Step 3, which can be
9 attributed to the diffusion of cations within the LTO lattice.
10

11 In particular, we focus on the processes corresponding to interface migration (Step 2) and bulk
12 diffusion (Step 3), which are closely related to the rate performance of batteries. Figure 4b depicts the
13 DRT spectra at the time scale corresponding to Step 3. With increasing temperature, the intensity of
14 the low-frequency DRT peak ($\tau \approx 10$ s) notably decreases, attributed to the thermal activation process
15 of lithium/sodium-ion migrations inside the LTO lattice (Step 3, bulk diffusion). In dual-cation
16 electrolytes, the impedance corresponding to bulk diffusion is smaller, indicating a higher cation
17 diffusion rate within the LTO lattice, which may be due to the sodium ions entering the crystal lattice
18 and promoting the diffusion of cations[24]. This is consistent with the AIMD simulation results in
19 Figures 3e-g. Moreover, the relaxation time and impedance at the interface in the single-cation system
20 initially decrease and then increase upon the temperature increase, as shown in Figure 4c. This
21 phenomenon can be due to the temperature-dependent cation diffusion rate within the solid-electrolyte
22 interface (SEI) layer. Comparing the LTO-electrolyte interface impedances of single-cation and dual-
23 cation electrolyte systems, we find that the addition of Na^+ leads to larger relaxation times and higher
24 impedances. This could be caused by the differences in the composition of the SEI layer formed in
25 different electrolyte systems.
26

27 In summary, the relaxation time for lithium/sodium-ion transport across the LTO-electrolyte interface
28 is approximately 0.1-1 s, while the diffusion time scale within the LTO lattice bulk is around 1-10 s.
29 The most significant difference between the two electrolyte systems during charging and discharging
30 lies in the addition of sodium ions that reduce the impedance of ion bulk diffusion within the LTO
31 lattice, and the different SEI compositions formed on the LTO electrode surface may also affect the
32 rate performance. Therefore, further investigation into the differences in interfacial properties between
33 the two electrolyte systems underscores the importance of studying the de-solvation processes and the
34 compositions of SEI films.
35

3.5 Effect of cation solvation structure and interfacial chemistry (SEI) of single/dual-cation electrolytes on the electrochemical performance of LTO

To further confirm the effect of cation solvation structures of single/dual-cation electrolytes on the electrochemical performance of LTO, we study the cation solvation structure of the single/dual-cation electrolytes using the 1M concentration electrolytes with the $\text{Li}^+ : \text{Na}^+$ ratio of 10: 0, 7: 3, 6: 4, 5: 5, 4: 6, 3: 7 via FTIR spectroscopy.

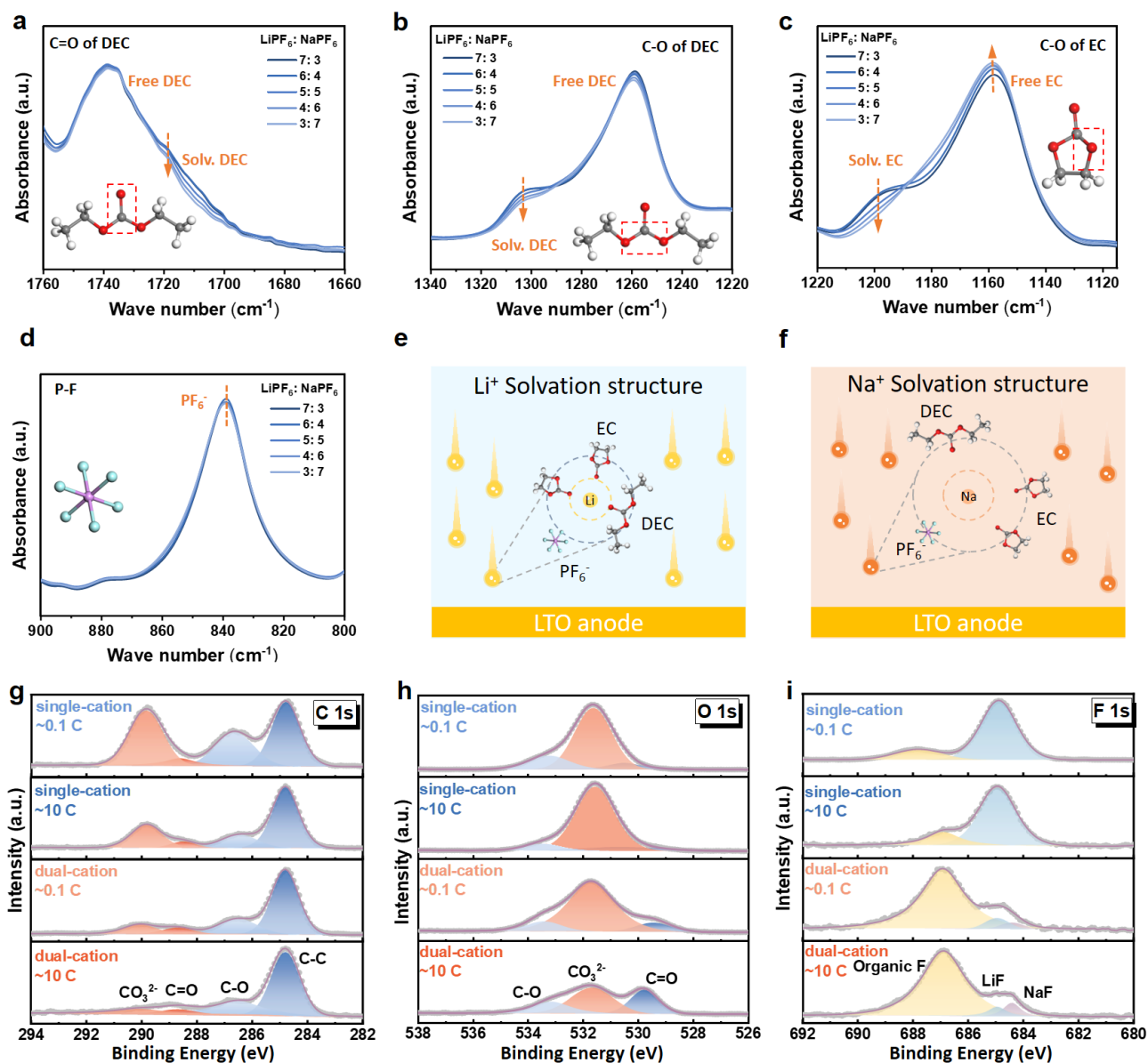


Figure 5 FTIR spectra of (a) C=O vibration peak of DEC molecule, (b) C-O vibration peak of DEC molecule, (c) C-O vibration peak of EC molecule and (d) P-F bond vibration peak of the dual-cation electrolytes with different $\text{Li}^+ : \text{Na}^+$ ratios. The schematic diagrams of (e) Li^+ and (f) Na^+ solvation structures in the dual-cation electrolytes. XPS spectra of (g) C 1s, (h) O 1s, and (i) F 1s peaks on the LTO surface after fast (~10 C) and slow (~0.1 C) charging processes in the two electrolyte systems.

1
2
3
4
5
6
7
8
9
10
11
12
13
14
15
16
17
18
19
20
21
22
23
24
25
26
27
28
29
30
Figures 4a-c show the FTIR peaks related to the C-O and C=O vibrations of DEC and EC solvent molecules, and the P-F vibration-related peaks are shown in Figure 4d. Through the analysis of the vibrational mode of the DEC solvent molecules, we found that with the addition of sodium ions, the characteristic peak intensities of the solvated C=O (Figure 5a) and C-O (Figure 5b) of DEC is decreased, indicating the decrease of the proportion of Li^+/Na^+ solvated DEC molecules. Similarly, the proportion of cation-solvated EC molecules also decreases significantly, meanwhile, the proportion of free EC molecules increases (Figure 5c). This may be because of the weak coordination interaction between solvent molecules and sodium ions compared with lithium ions[38]. As a result, with the increase of Na^+ contents in the electrolyte, the proportion of coordinated EC and DEC solvent molecules are both decreased, confirming a lower de-solvation energy of the cation in the dual-cation electrolyte. It is also worth noting that anions barely participate in the primary solvation shell, therefore the P-F peak does not vary with the changes in the $\text{Li}^+:\text{Na}^+$ ratio (Figure 5d). However, according to the DRT measurements in Figure 4c, the impedance of cations in the process of crossing the LTO-electrolyte interface in dual-cation electrolyte is larger than that of single-cation electrolyte, which should lead to a decreased reversible capacity at a high charge/discharge rate. This implied that not only the de-solvation energy but also the diffusion of cations crossing the SEI layer should be taken into consideration.

31
32
33
34
35
36
37
38
39
40
41
42
43
44
45
46
47
48
49
50
51
52
53
54
55
56
The interfacial chemistries of the LTO half-cells charged/discharged at ~ 0.1 C and ~ 10 C current densities in single-cation and dual-cation electrolytes were further studied by XPS. After 10 cycles, the cells were disassembled and cleaned with diethyl carbonate (DEC) solvent, and then the SEI components on the electrode surface were tested by XPS. As shown in Figures 5g-I, the main SEI components formed on the LTO surface seem to be independent of the charge/discharge rates, while they are highly dependent on the electrolyte components. From the C 1s XPS spectra in Figure 5g, we found there are fewer $\text{CO}_3^{2-}/\text{C}=\text{O}/\text{C}-\text{O}$ related SEI compounds on the LTO surface cycled in the dual-cation electrolyte compared to the LTO electrolyte cycled in the single-cation electrolyte, which is also consistent with the results observed in the O 1s spectra in Figure 5h. However, the peak intensity of fluoride organic SEI compounds is significantly high on the LTO electrode surface after cycling in the dual-cation electrolyte (Figure 5i). This organic compound dominates the composition of the SEI film formed in dual-cation electrolyte, which may result in a large interfacial impedance as revealed by the DRT spectra in Figure 4c. Therefore, optimization strategies may be taken in regulating the SEI components in dual-cation electrolytes for further enhancing the overall electrochemical performance.

57 58 59 60 61 62 63 64 65 **4. Conclusion**

In this study, a binder-free LTO thin film electrode was prepared as the model electrode to study the

1 charge storage mechanisms of LTO in the dual-cation electrolyte. The electrochemical measurements
2 show that part of the capacity of LTO in the dual-cation electrolyte system derives from the
3 intercalation of sodium ions, and the additional capacity may derive from the pseudo-capacitance effect
4 at the electrode surface, defects and the sodium occupation at the 48f sites. The dynamic evolutions of
5 the sodium/lithium-ion occupancy states in the dual-cation electrolyte were studied by non-destructive
6 *operando* Raman spectroscopy, which revealed that the sodium ion initially occupied the 8a sites, and
7 then moved to the 16c sites at the end of intercalation. AIMD simulation confirmed that the Na⁺
8 dopants reduce the activation energy of cation migrations within the LTO crystal lattice, which can
9 effectively increase the cation diffusion coefficient as conformed by the reduced DRT peak intensity
10 in the large-time constant region. Moreover, the origin of high-rate performance limitation factors in
11 the dual-cation electrolyte was also studied in detail. FTIR and XPS measurements support that the
12 electrolyte with Na⁺ (dual-cation electrolyte) shows reduced de-solvation energy, while the obtained
13 SEI component contains more organic fluoride components that are deconstructive to the cation
14 shuttling through the electrode-electrolyte interfaces, impeding the fast charge transform process of
15 LTO anodes. Our results provide insights into the impact of the de-solvation process and the derived
16 SEI components on further optimizing the dual-cation electrolytes and prospects for the electrolyte
17 engineering approaches of other batteries with similar chemistries.

33 **Acknowledgements**

34 This work was financially supported by the National Natural Science Foundation of China (Nos.
35 61574037, 11874113, and 52172243), Faraday Institution (grant number FIRG018), EU Graphene
36 Flagship Core 3 project, EPSRC project EP/V00767X/1 and the Science Foundation of the Fujian
37 Province (No. 2023J01521). D.Z. acknowledges the receipts of a Sydney Andrew Scholarship from
38 the Society of Chemical Industry and a Chinese Students Award from the Great Britain-China
39 Educational Trust (GBCET).

46 **References**

- 47 [1] Z. Hao, Y. Yang, X. Hong, W. Li, L. Xia, X. He, Li₄Ti₅O₁₂ spinel anode: Fundamentals and
48 advances in rechargeable batteries, *InfoMat* 4(4) (2021).
49 [2] C. Han, Y.-B. He, S. Wang, C. Wang, H. Du, X. Qin, Z. Lin, B. Li, F. Kang, Large Polarization of
50 Li₄Ti₅O₁₂ Lithiated to 0 V at Large Charge/Discharge Rates, *ACS Appl. Mater. Interfaces* 8(29) (2016)
51 18788-18796.
52 [3] S. Fu, X. Yu, Q. Wu, X. Yang, Z. Liu, X. Li, S. He, D. Wang, Y. Li, S. Tong, M. Wu, Ultrathin
53 [110] - Confined Li₄Ti₅O₁₂ Nanoflakes for High Rate Lithium Storage, *Advanced Energy Materials*
54 11(22) (2021).
55 [4] F. Zhao, P. Xue, H. Ge, L. Li, B. Wang, Na-Doped Li₄Ti₅O₁₂ as an Anode Material for Sodium-
56 Ion Battery with Superior Rate and Cycling Performance, *Journal of The Electrochemical Society*
57
58
59
60

163(5) (2016) A690-A695.

[5] S. Ganapathy, A. Vasileiadis, J.R. Heringa, M. Wagemaker, The Fine Line between a Two - Phase and Solid - Solution Phase Transformation and Highly Mobile Phase Interfaces in Spinel $\text{Li}_{4+x}\text{Ti}_5\text{O}_{12}$, *Advanced Energy Materials* 7(9) (2016) 1601781.

[6] L. Hou, X. Qin, X. Gao, T. Guo, X. Li, J. Li, Zr-doped $\text{Li}_4\text{Ti}_5\text{O}_{12}$ anode materials with high specific capacity for lithium-ion batteries, *Journal of Alloys and Compounds* 774 (2019) 38-45.

[7] S.H. Gong, J.H. Lee, D.W. Chun, J.-H. Bae, S.-C. Kim, S. Yu, S. Nahm, H.-S. Kim, Effects of Cr doping on structural and electrochemical properties of $\text{Li}_4\text{Ti}_5\text{O}_{12}$ nanostructure for sodium-ion battery anode, *Journal of Energy Chemistry* 59 (2021) 465-472.

[8] P. Yu, C. Li, X. Guo, Sodium Storage and Pseudocapacitive Charge in Textured $\text{Li}_4\text{Ti}_5\text{O}_{12}$ Thin Films, *The Journal of Physical Chemistry C* 118(20) (2014) 10616-10624.

[9] Q. Guo, X. Cheng, Y. Shi, Z. Sheng, C. Chang, Bluish $\text{Li}_4\text{Ti}_5\text{O}_{12}$ with enhanced rate performance, *Journal of Alloys and Compounds* 710 (2017) 383-392.

[10] D.M. Cunha, T.A. Hendriks, A. Vasileiadis, C.M. Vos, T. Verhallen, D.P. Singh, M. Wagemaker, M. Huijben, Doubling Reversible Capacities in Epitaxial $\text{Li}_4\text{Ti}_5\text{O}_{12}$ Thin Film Anodes for Microbatteries, *ACS Appl. Mater. Interfaces* 2(5) (2019) 3410-3418.

[11] M. Kalapsazova, H. Rasheev, E. Zhecheva, A. Tadjer, R. Stoyanova, Insights into the Function of Electrode and Electrolyte Materials in a Hybrid Lithium–Sodium Ion Cell, *The Journal of Physical Chemistry C* 123(18) (2019) 11508-11521.

[12] C. Jiang, Y. Fang, W. Zhang, X. Song, J. Lang, L. Shi, Y. Tang, A Multi-Ion Strategy towards Rechargeable Sodium-Ion Full Batteries with High Working Voltage and Rate Capability, *Angewandte Chemie* 57(50) (2018) 16370-16374.

[13] A. Ghosh, F. Ghamouss, Role of Electrolytes in the Stability and Safety of Lithium Titanate-Based Batteries, *Frontiers in Materials* 7 (2020).

[14] M. Kitta, R. Kataoka, S. Tanaka, N. Takeichi, M. Kohyama, Spinel-Type Sodium Titanium Oxide: A Promising Sodium-Insertion Material of Sodium-Ion Batteries, *ACS Appl. Mater. Interfaces* 2(6) (2019) 4345-4353.

[15] H.R. Yao, Y. You, Y.X. Yin, L.J. Wan, Y.G. Guo, Rechargeable dual-metal-ion batteries for advanced energy storage, *Phys Chem Chem Phys* 18(14) (2016) 9326-33.

[16] Q. Liu, H. Wang, C. Jiang, Y. Tang, Multi-ion strategies towards emerging rechargeable batteries with high performance, *Energy Storage Materials* 23 (2019) 566-586.

[17] L. Zhao, H.-L. Pan, Y.-S. Hu, H. Li, L.-Q. Chen, Spinel lithium titanate ($\text{Li}_4\text{Ti}_5\text{O}_{12}$) as novel anode material for room-temperature sodium-ion battery, *Chinese Phys B* 21(2) (2012).

[18] Y. Sun, L. Zhao, H.L. Pan, X. Lu, L. Gu, Y.S. Hu, H. Li, M. Armand, Y. Ikuhara, L.Q. Chen, X.J. Huang, Direct atomic-scale confirmation of three-phase storage mechanism in $\text{Li}_4\text{Ti}_5\text{O}_{12}$ anodes for room-temperature sodium-ion batteries, *Nat. Commun.* 4(1) (2013) 1870.

[19] X. Feng, H. Zou, H. Xiang, X. Guo, T. Zhou, Y. Wu, W. Xu, P. Yan, C. Wang, J.G. Zhang, Y. Yu, Ultrathin $\text{Li}_4\text{Ti}_5\text{O}_{12}$ Nanosheets as Anode Materials for Lithium and Sodium Storage, *ACS Appl. Mater. Interfaces* 8(26) (2016) 16718-26.

[20] S. Natarajan, K. Subramanyan, V. Aravindan, Focus on Spinel $\text{Li}_4\text{Ti}_5\text{O}_{12}$ as Insertion Type Anode for High - Performance Na - Ion Batteries, *Small* 15(49) (2019) 1904484.

[21] K. Mukai, Y. Kato, H. Nakano, Understanding the Zero-Strain Lithium Insertion Scheme of $\text{Li}[\text{Li}_{1/3}\text{Ti}_{5/3}]\text{O}_4$: Structural Changes at Atomic Scale Clarified by Raman Spectroscopy, *The Journal of Physical Chemistry C* 118(6) (2014) 2992-2999.

[22] M. Kitta, M. Kohyama, Mechanism of the Na-substituted Spinel Phase Generation in a $\text{Li}_4\text{Ti}_5\text{O}_{12}$ Electrode via Sodium-ion Battery Cycling, *Electrochemistry* 86(4) (2018) 194-197.

[23] J. Li, X. Chang, T. Huang, B. Wang, H. Zheng, Q. Luo, D.-L. Peng, Q. Wei, Surface-controlled sodium-ion storage mechanism of $\text{Li}_4\text{Ti}_5\text{O}_{12}$ anode, *Energy Storage Materials* 54 (2023) 724-731.

[24] P. Posch, S. Lunghammer, A. Wilkening, K. Hogrefe, H.M.R. Wilkening, Understanding fast ion

1 dynamics in sodiated $\text{Li}_4\text{Na}_x\text{Ti}_5\text{O}_{12}$: from interfacial to extended Li^+ and Na^+ dynamics in its mixed-
2 conducting solid solutions, *Journal of Physics: Energy* 5(1) (2022).

3 [25] M. Kitta, R. Kataoka, M. Kohyama, Study of the interface between Na-rich and Li-rich phases in
4 a Na-inserted spinel $\text{Li}_4\text{Ti}_5\text{O}_{12}$ crystal for an electrode of a sodium-ion battery, *Physical Chemistry
5 Chemical Physics* 18(29) (2016) 19888-19893.

6 [26] M. Kitta, T. Akita, S. Tanaka, M. Kohyama, Two-phase separation in a lithiated spinel $\text{Li}_4\text{Ti}_5\text{O}_{12}$
7 crystal as confirmed by electron energy-loss spectroscopy, *Journal of Power Sources* 257 (2014) 120-
8 125.

9 [27] The carrier transition from Li atoms to Li vacancies in solid-state lithium alloy anodes.

10 [28] Z. Li, W. Zhang, Y. Chen, Q. Lin, L. Zhang, J. Tao, O.V. Kolosov, J. Li, Y. Lin, Z. Huang,
11 Enhancing interfacial Li^+ transport and dielectric properties in poly(ethylene oxide)-based all-solid
12 electrolytes via inactive g-C₃N₄ nanosheets filler incorporation, *Journal of Materials Science &
13 Technology* 183 (2024) 184-192.

14 [29] Y. Zhang, Y. Chen, M. Yan, F. Chen, Reconstruction of relaxation time distribution from linear
15 electrochemical impedance spectroscopy, *Journal of Power Sources* 283 (2015) 464-477.

16 [30] B. Deng, P. Zhong, K. Jun, J. Riebesell, K. Han, C.J. Bartel, G. Ceder, CHGNet as a pretrained
17 universal neural network potential for charge-informed atomistic modelling, *Nature Machine
18 Intelligence* 5(9) (2023) 1031-1041.

19 [31] E. Proskuryakova, O. Kondratov, N. Porotnikov, K.J.Z.N.K. Petrov, Vibrational-spectra of lithium
20 titanate with a spindle structure, 28(6) (1983) 1402-1406.

21 [32] I.A. Leonidov, O.N. Leonidova, L.A. Perelyaeva, R.F. Samigullina, S.A. Kovyazina, M.V.
22 Patrakee, Structure, Ionic Conduction, and Phase Transformations in Lithium Titanate $\text{Li}_4\text{Ti}_5\text{O}_{12}$, *Phys.
23 Soild State* 45(11) (2003) 2183-2188.

24 [33] H. Liu, Z. Zhu, J. Huang, X. He, Y. Chen, R. Zhang, R. Lin, Y. Li, S. Yu, X. Xing, Q. Yan, X. Li,
25 M.J. Frost, K. An, J. Feng, R. Kosteccki, H. Xin, S.P. Ong, P. Liu, Elucidating the Limit of Li Insertion
26 into the Spinel $\text{Li}_4\text{Ti}_5\text{O}_{12}$, *ACS Materials Letters* 1(1) (2019) 96-102.

27 [34] Y. Sun, L. Zhao, H. Pan, X. Lu, L. Gu, Y.S. Hu, H. Li, M. Armand, Y. Ikuhara, L. Chen, X. Huang,
28 Direct atomic-scale confirmation of three-phase storage mechanism in $\text{Li}_4\text{Ti}_5\text{O}_{12}$ anodes for
29 room-temperature sodium-ion batteries, *Nature communications* 4 (2013) 1870.

30 [35] J. Wang, J. Polleux, J. Lim, B. Dunn, Pseudocapacitive Contributions to Electrochemical Energy
31 Storage in TiO_2 (Anatase) Nanoparticles, *Journal of Physical Chemistry C* 111 (2007) 14925-14931.

32 [36] Q. Wei, X. Chang, D. Butts, R. DeBlock, K. Lan, J. Li, D. Chao, D.L. Peng, B. Dunn, Surface-
33 redox sodium-ion storage in anatase titanium oxide, *Nat. Commun.* 14(1) (2023) 7.

34 [37] Q. Wei, X. Chang, D. Butts, R. DeBlock, K. Lan, J. Li, D. Chao, D.-L. Peng, B. Dunn, Surface-
35 redox sodium-ion storage in anatase titanium oxide, *Nature communications* 14(1) (2023).

36 [38] A.V. Cresce, S.M. Russell, O. Borodin, J.A. Allen, M.A. Schroeder, M. Dai, J. Peng, M.P. Gobet,
37 S.G. Greenbaum, R.E. Rogers, K. Xu, Solvation behavior of carbonate-based electrolytes in sodium
38 ion batteries, *Phys Chem Chem Phys* 19(1) (2016) 574-586.

Declaration of interests

The authors declare that they have no known competing financial interests or personal relationships that could have appeared to influence the work reported in this paper.

The authors declare the following financial interests/personal relationships which may be considered as potential competing interests: